Intensity-resolved above-threshold ionization of xenon with short laser pulses

N. A. Hart,[1,*] J. Strohaber,[1,2] G. Kaya,[1] N. Kaya,[1] A. A. Kolomenskii,[1] and H. A. Schuessler[1]
[1]*Department of Physics, Texas A&M University, College Station, Texas 77843-4242, USA*
[2]*Department of Physics, Florida A&M University, Tallahassee, Florida 32307, USA*
(Received 29 January 2014; published 15 May 2014)

We present intensity-resolved above-threshold ionization (ATI) spectra of xenon using an intensity scanning and deconvolution technique. Experimental data were obtained with laser pulses of 58 fs and a central wavelength of 800 nm from a chirped-pulse amplifier. Applying a deconvolution algorithm, we obtained spectra that have higher contrast and are in excellent agreement with characteristic two and ten U_p cutoff energies contrary to that found for raw data. The retrieved electron-ionization probability is consistent with the presence of a second electron from double ionization. This recovered ionization probability is confirmed with a calculation based on the Perelomov, Popov, and Terent'ev tunneling ionization model [Sov. Phys. JETP **23**, 924 (1966)]. Thus, the measurements of the photoelectron yields and the developed deconvolution technique allowed retrieval of more accurate spectroscopic information from the ATI spectra and ionization probability features that usually are concealed by volume averaging.

DOI: 10.1103/PhysRevA.89.053414 PACS number(s): 32.80.Rm, 32.80.Fb, 32.90.+a, 42.50.Hz

I. INTRODUCTION

The focal volume of a laser beam contains a continuum of intensities that vary both radially and longitudinally with respect to the axis of propagation and range from zero to some peak intensity I_0. Each intensity provides a unique ion yield contribution depending on the probability of ionization $P(I)$ and the volume occupied by the radiation at that intensity. This results in an averaging effect that ultimately reduces the intensity resolution of an experimental measurement [1]. This lack of resolution masks intensity-dependent phenomena, such as the ionization probability, ac-Stark shifts, and Rabi oscillations in the atomic energy levels [2]. It has been shown that ions can be distinguished according to their location in the laser focus from which they are produced [3]. But although higher ionization states A^{+n} have been observed in ion time-of-flight (TOF) measurements [1,3], to the best of our knowledge, the explicit manifestation of photoelectrons specific to a charge state greater than one has not been observed. The difficulty of such detection follows from the fact that measuring devices rarely are able to determine the location within the focus that an electron originated from. Insufficient temporal resolution results in integration of the signal over the entire focal volume of the laser. For instance, distinguishing two electrons in a field-free region each with 1.5 eV of kinetic energy and a separation distance of 10 μm would require data-acquisition electronics with 13-ps temporal resolution. However, fast data-acquisition electronics have timing resolutions of a few hundred picoseconds.

Theoretical calculations for laser-matter interactions typically are carried out using plane waves of coherent radiation with some time-dependent amplitude modulation [4,5], and the probability of ionization is determined after the interaction. Because, in practice, ionization experiments with short laser pulses record the ionization yield after the pulse has interacted with the target and because experimental results are spatially averaged, theoretically determined ionization probabilities are averaged artificially for comparison with experiments. The need to compare with the more fundamental nonspatially averaged theoretical results has motivated the design of intensity-resolved experiments. In them, the goal is to remove the influence of the spatially varying intensity distribution from laser beam modes and isolate the result of a single intensity. Hansch and Van Woerkom [6] used a slit to collect ions from a small cross-sectional area of the laser focus. The novelty of their approach was that they varied the intensity in which the detected ions were born by changing the position of the slit along the z axis relative to the laser focus. Walker *et al.* [7] coupled this measurement with an algorithm that removes the effect of radial variation in the laser intensity. This combined technique is known as intensity selective scanning (ISS). Bryan *et al.* [8] modified ISS by accounting for diffraction effects along the z axis of the laser focus.

Goodworth *et al.* [9] developed a deconvolution scheme which used discretized isointensity rings of the two-dimensional cross sections of the laser focus. An off-axis slit aligned perpendicular to the z axis determined the width of these cross sections from which the ions were collected. The volume of each isointensity ring was represented by a matrix element $V_{n,s}$ where n indexes the z-axis position and s indexes the intensity of the ring. Deconvolution, to obtain a probability P_s, was carried out by an inverse matrix $V_{s,n}^{-1}$ multiplication of the yields Y_n from the z-scanned measurement: $P_s = V_{s,n}^{-1} Y_n$.

Other methods have employed purely experimental techniques to measure ions from an isointensity volume of the laser focus, which is confined in all three spatial dimensions. Schultze *et al.* [10] and Strohaber and Uiterwaal [3] used an imaging TOF spectrometer to sort positive ions from the focus. Ions created at different locations within the focus arrive at a detector at different times. In their experiments, arrival times coupled with longitudinal and transverse measurements provide the ability to both reconstruct the spatial isointensity shells of the laser focus and extract intensity-resolved ionization probabilities from intensity scans.

Strohaber *et al.* [11] introduced the multiphoton expansion as an analytical deconvolution of the laser focal volume by

*Corresponding author: nhart@physics.tamu.edu

solving the linear Volterra equation of the first kind. The solution for the ionization probability is represented by a power series of the intensity suggesting the name of this approach. The Volterra integral represented the total number of ions detected from an N-dimensional ($N = 1$, 2, or 3) volume within the focus. As such, this approach allows for the deconvolution of a variety of intensity scanning experimental schemes.

In the present paper, we developed a generalized algorithmic technique to recover intensity-resolved above-threshold ionization (ATI) energy spectra using photoelectrons; additionally, this technique may also be used for other spatially averaged data. The technique involves obtaining ATI measurements using short laser pulses of different peak intensities and employing a deconvolution algorithm to remove the blurring effect of the spatially varying intensities. The results of this procedure revealed the presence of an electron from a second ionization and an unanticipated and unreported shift in the cutoff energies.

II. DISCRETE DECONVOLUTION AND REGULARIZATION

The measured ionization yield of an atom $Y(I_0)$ can be expressed as a convolution of the ionization probability per unit volume $P(I)$ and the derivative of the volume $V(I_0,I)$ enclosing all intensities greater than I up to a maximum or peak intensity I_0,

$$Y(I_0) = \int_0^{I_0} P(I) \left| \frac{\partial V(I_0,I)}{\partial I} \right| dI, \tag{1}$$

where $V(I_0,I)$ contains the geometric information about the focal region being measured. Thus, it is implicitly dependent on the optics used and any apertures between the interaction region and the signal detector. The functional form of $V(I_0,I)$ in one, two, and three dimensions is given in Strohaber *et al.* [11].

To deconvolve the ionization probability $P(I)$ from Eq. (1), the experiment must be repeated more than once using different peak intensities. Therefore, we introduce the notation I_n to denote the peak intensity of the laser beam in the nth experiment. We will now construct a numerical approximation of Eq. (1). Note that the magnitude of both $V(I_n,I)$ and its I derivative become infinite as I approaches zero. Therefore, the lower limit of Eq. (1) is computationally impractical, and the interval of integration will need to be truncated by a parameter $\delta I \ll I_n - \delta I$,

$$\begin{aligned} Y(I_n) &= \int_0^{\delta I} P(I) \left| \frac{\partial V(I_n,I)}{\partial I} \right| dI + \int_{\delta I}^{I_n} P(I) \left| \frac{\partial V(I_n,I)}{\partial I} \right| dI \\ &\approx \int_{\delta I}^{I_n} P(I) \left| \frac{\partial V(I_n,I)}{\partial I} \right| dI. \end{aligned} \tag{2}$$

As I_n increases, the integral over the interval $[\delta I, I_n]$ more accurately approximates the full integral over $[0, I_n]$. Since the ionization probability $P(I)$ tends to decay with decreasing intensity, this also reduces the introduced approximation error.

To estimate Eq. (2) numerically, we can discretize the integral using a Riemann sum. The integration interval is partitioned by introducing an ordered set of intensities $I_s \in \{I_1, I_2, \ldots, I_N\}$ such that $I_1 > I_2 > \cdots > I_N > \delta I$. Note that our choice of notation for I_n deliberately restricts the set of peak intensities at which we experimentally measure the yield $Y(I_n)$. Since $V(I_n,I_s)$ monotonically increases with decreasing I_s, the volume $V(I_n,\delta I)$ is also implicitly partitioned. We can, therefore, introduce differential volume elements $\Delta V = V_{n,s}$ for the set I_s at a peak intensity I_n to approximate Eq. (2),

$$\begin{aligned} \int_{\delta I}^{I_n} P(I) \left| \frac{\partial V(I_n,I)}{\partial I} \right| dI &= \lim_{N\to\infty} \sum_{s=n}^{N} V_{n,s} P(I_s) \\ &\approx \sum_{s=n}^{N} V_{n,s} P(I_s). \end{aligned} \tag{3}$$

$V_{n,s}$ and the corresponding Riemann sum can be defined in a number of different ways (midpoint rule, trapezoidal rule, Simpsons rule, etc . . .). However, any definition of $V_{n,s}$ must satisfy

$$\sum_{s=n}^{N} V_{n,s} = V(I_n,\delta I), \tag{4}$$

meaning that the sum of all differential volume elements must equal the total volume enclosed by the smallest intensity δI. Moreover, to obtain a good approximation to Eq. (3), the condition $V_{n,s} \ll V(I_n,\delta I)$ should be satisfied for all s. We chose, for simplicity, to define $V_{n,s}$ by taking the difference between the volumes enclosed by two consecutive isointensity shells,

$$V_{n,s} \equiv \begin{cases} |V(I_n,I_{s+1}) - V(I_n,I_s)| \to s \geqslant n, \\ 0 \to s < n. \end{cases} \tag{5}$$

This definition follows from the discrete first derivative of the volume,

$$\frac{\Delta V(I_n,I_s)}{\Delta I} \Delta I = \frac{V(I_n,I_s) - V(I_n,I_{s+1})}{I_s - I_{s+1}} (I_s - I_{s+1}), \tag{6}$$

and is equivalent to taking a right Riemann sum.

If the indices n and s have the same dimensions ($n,s \in \{1,2,\ldots,N\}$), Eq. (3) produces a system of linear equations that can be expressed in matrix form as $\boldsymbol{Y} = \hat{V} \cdot \boldsymbol{P}$, where $\hat{V} \equiv V_{n,s}$ denotes the differential volume matrix, $\boldsymbol{P} \equiv (P(I_1), P(I_2), \ldots, P(I_N))^T$ is the probability array, and $\boldsymbol{Y} \equiv (Y(I_1), Y(I_2), \ldots, Y(I_N))^T$ is the signal yield array. Solving for the ionization probability per unit volume $\boldsymbol{P}$, we obtain

$$\boldsymbol{P} = \hat{V}^{-1} \cdot \boldsymbol{Y} = (\hat{V}^T \hat{V})^{-1} \hat{V}^T \cdot \boldsymbol{Y}. \tag{7}$$

A one-dimensional example illustrating the construction of Eq. (7) is presented in Appendix A.

Since I_N would be the smallest element in the list of measured intensities, a free parameter $I_{N+1} \equiv \delta I$ must be chosen for the calculation of an outermost volume $V(I_n, I_{N+1})$ for all n (see Fig. 1). The choice of the free parameter $I_{N+1} = \delta I$ in Eq. (3) can be determined from $V_{N,N} = Y(I_N)/P(I_N)$, which assumes some knowledge of the probability $P(I_N)$. We note that, for some simple atoms in the multiphoton regime, the probability $P(I_N)$ can be determined theoretically using perturbation theory [12]. It is known that the multiphoton yield at low intensities is proportional to the probability, since

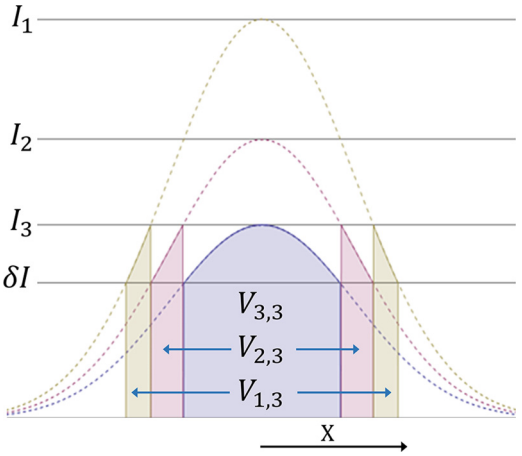

FIG. 1. (Color online) An example schematic in one dimension showing how volume elements are related to peak intensities. Here the total number of experiments is $N = 3$. The boundary of each volume (horizontal) is set by intensities δI and I_3. δI is a free parameter that provides an outer boundary for the calculation of the volume elements. The central blue region represents $V_{3,3}$, the sandwiched red regions are $V_{2,3}$, and the outer gold regions are $V_{1,3}$. Each of these three volumes corresponds to the same ionization probability $P(I_3)$.

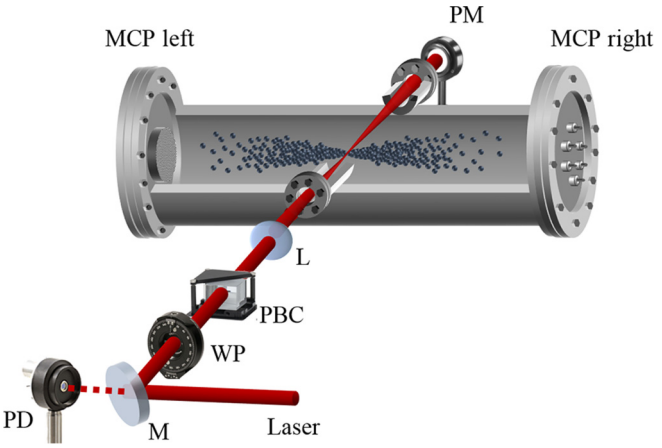

FIG. 2. (Color online) Experimental setup: M: mirror; WP: half-wave plate; PD: photodiode; PBC: polarizing beam-splitter cube; L: lens; MCP: chevron microchannel plate; PM: power meter.

the highest intensity of the beam dominates the signal. We, therefore, determine δI by requiring that the derivatives of the probability and yield are equal at I_N, i.e., $\Delta P/\Delta I = \Delta Y/\Delta I_0$.

It is important to note that, in practice, the inversion in Eq. (7) is unstable with small variations in the yield $\boldsymbol{Y}$. However, by implementing a modified version of the variation minimization algorithms proposed by Le *et al.* [13] and Chartrand and Wohlberg [14], we are able to introduce a regularization term to the right hand side of Eq. (7) to obtain the regularized probability $\bar{\boldsymbol{P}}_i$,

$$\bar{\boldsymbol{P}}_i = (\hat{V}^T \hat{V} - 2\beta \hat{M}_i \hat{\nabla}^2)^{-1} \hat{V}^T \boldsymbol{Y}. \tag{8}$$

A more detailed discussion of the regularization algorithm, including the regularization term $2\beta \hat{M}_i \hat{\nabla}^2$, and the iteration subscript i are discussed in Appendix B. The iteration of Eq. (8) and its regularization term to find $\bar{\boldsymbol{P}}_i$ hereafter is referred to as the discrete deconvolution and regularization (DDAR) algorithm.

III. EXPERIMENTAL SETUP

The ATI apparatus is depicted in Fig. 2. Target xenon atoms were ionized with short laser pulses. A series of ionization measurements was taken for 120 different peak laser intensities ranging within $3 \times 10^{13} - 8 \times 10^{14}$ W/cm^2. All other laser parameters, such as mode quality, pulse duration, and spectral bandwidth were unchanged.

The Ti:sapphire laser oscillator provides 20-fs mode-locked laser pulses at a repetition rate of 80 MHz. These pulses are seeded into a regenerative laser amplifier, which outputs 58-fs (measured by frequency resolved optical gating, GRENOUILLE 8-20, Swamp Optics, LLC) laser pulses at a repetition rate of 1 kHz, and a central wavelength of 800 nm. Since shorter pulses have a higher peak intensity for a given pulse energy, temporal compression of the laser pulses in the focus was achieved by maximizing the integrated photoelectron yield in the ATI apparatus by adjusting the grating compressor in the laser amplifier. The maximum pulse energy was approximately 0.8 mJ.

Laser pulses were detected before the half-wave plate of the attenuator by a photodiode, and the signal was used to trigger the data-acquisition software. The attenuator consisted of a half-wave plate that changed the polarization of the initially horizontally polarized light and a polarizing cube that filtered out vertically polarized light while horizontally polarized light passed through. The orientation of the wave plate was varied such that, after the polarizing cube, the desired intensity is achieved in the laser focus.

The vacuum chamber was filled with xenon gas of 99.999% purity (Advanced Specialty Gasses) through a variable leak valve. The xenon pressure (5×10^{-6} mbar) was three orders of magnitude higher than the background pressure in the ionization chamber. Because the ionization potential of water (12.61 eV) is roughly equal to that of xenon (12.15 eV), a large-surface-area vacuum feedthrough, located on the TOF chamber, was chilled using liquid nitrogen to freeze out residual water molecules from the background vacuum. The laser beam was focused by a 20-cm achromatic lens. Ionized electrons were ejected along the polarization of the laser field in the direction of the microchannel plate (MCP) detector. The electrons traveled within a μ-metal TOF tube in a field-free region. Electrons from the entire focal volume of the laser were measured at the detector. The signals from the MCP were amplified by a high bandwidth Mini-Circuits ZKL-2 preamplifier before being registered by a FAST ComTec MCS6 multiscaler with 100-ps timing resolution. A power meter (PM) measured the average laser power, which is proportional to the average peak laser intensity in the focus.

The DDAR algorithm was written in *Mathematica* and was employed on an Intel i7 desktop computer having 16 GB of memory. The algorithm deconvolved the entire data set (a 19.0-MB matrix of raw electron TOF spectra) in 0.824 s.

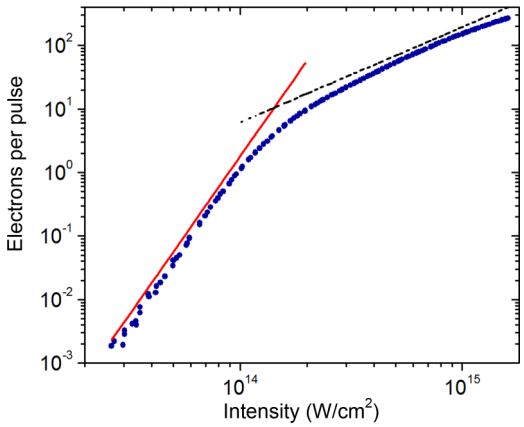

FIG. 3. (Color online) The experimentally measured electron yield $\boldsymbol{Y}$ on a log-log plot. Two slopes are plotted showing the intensity dependence: a slope of 5 (solid line) and a slope of 3/2 (dashed line). The change in slope occurs slightly above the saturation intensity $I_{\text{sat}} = 1.2 \times 10^{14}\text{W/cm}^2$.

IV. RESULTS

The electron-ionization yield as recorded along the laser polarization is shown in Fig. 3. The saturation intensity is measured to be $I_{\text{sat}} = 1.2 \times 10^{14}\text{W/cm}^2$. On a log-log plot, the yield curve shows a slope of 5 for intensities less than I_{sat} and a slope of 3/2 for intensities greater than I_{sat}. The slope of 3/2 arises from volumetric integration of the electrons ionized from all intensities in the Gaussian beam. As the peak intensity $I_0 \equiv I\,(r = 0)$ increases, the total volume enclosed by an intensity $I\,(r > 0) < I_0$ grows as $I_0^{3/2}$ [15]. As this volume grows, so does the yield, and the largest contribution to the yield after the saturation intensity comes from those intensities with the highest ionization probability.

One of the effects of using regularization is that the resulting yield $\bar{\boldsymbol{Y}}$ is smoother than the original data. This provides more stability to the retrieved probability $\bar{\boldsymbol{P}}$. Increasing the regularization parameter β strengthens the regularization and minimizes discontinuities in the derivative of $\bar{\boldsymbol{P}}$. Consequently, we used $\beta = 0.5$. Since $\bar{\boldsymbol{P}}$ is the ionization probability per unit volume, we divide it by the gas density (proportional to pressure) in the laser interaction region to obtain the ionization probability per atom. Electrons from different ion charge states have unique ionization probability functions that approach unity as intensity increases. However, these charge states have different saturation intensities. Hence, the graph of the probability first saturates (approaches 1) at $1.2 \times 10^{14}\text{W/cm}^2$ and then reaches a maximum value of 2 at approximately $2.7 \times 10^{14}\text{W/cm}^2$ (Fig. 4). This second saturation primarily is attributed to single ionization of the singly charged xenon ion. The MCP detector cannot distinguish between electrons from different charge states. Therefore, electron yields from both species and, by implication, their probabilities are summed giving a "stair step" appearance. In addition to the deconvolved experimental data, Fig. 4 also shows the results of a PPT tunneling ionization simulation [16]. The red curve is the result of summing the calculated ionization probability of both the Xe^+ and Xe^{2+} ions, whereas, the blue curve exclusively represents the Xe^{2+} ionization probability.

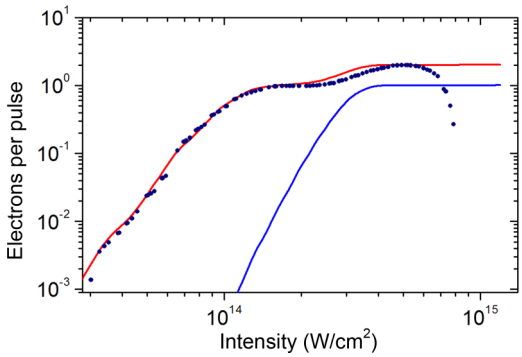

FIG. 4. (Color online) Recovered electron probability on a log-log plot (dotted line). The red curve is a Perelomov, Popov, and Terent'ev (PPT) theory simulation of the xenon probability for electron yields for Xe^{1+} and Xe^{2+}. The blue curve shows the simulation of the electron yield probability for Xe^{2+} electrons alone. The deconvolution diverges at the high intensity end point.

Even though the signal shows significant noise, DDAR still recovers the probability. Multiple ionization of Xe has been measured by other groups using ion, but not electron, detection as in this experiment and compares favorably with our results [1]. The counting electronics naturally groups the electrons according to when they arrive or by their TOF. By transforming this time series into an energy spectrum and applying DDAR to the yield rates for each electron energy, the intensity-resolved (volume-independent) energy spectra are obtained. One such spectrum is plotted in Fig. 5.

For the following discussion of features in the ATI spectra, see Fig. 5. The first plateau between 0 and 8 eV is the result of "direct" electrons that do not scatter off the parent ion after being ionized. These electrons have a classical cutoff energy of $2U_p$, where U_p is the ponderomotive energy of the laser field [17]. In this low-energy region, REMPI is expected to dominate the ATI peak structure (inset) [18]. The second plateau between 12 and 25 eV is dominated by

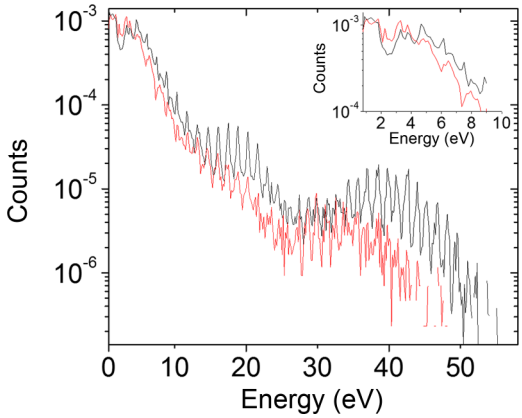

FIG. 5. (Color online) Intensity-resolved ATI energy spectra at 8.7×10^{13} W/cm^2 of electrons per laser pulse. The red curve is the measured data prior to being deconvolved. The deconvolution shows more pronounced features. The inset shows the $2U_p$ low-energy region of the same data. Resonantly enhanced multiphoton ionization (REMPI) peaks can be seen at energies less than 4 eV.

the interference of electrons which follow different quantum trajectories and are freed with an initially near-zero velocity by either tunneling ionization or resonant multiphoton ionization at a channel closing [19]. This ionization mechanism also makes the second plateau important for the study of high harmonic generation [20]. As electrons are accelerated by the electric field, the different quantum paths of electrons with equal momenta can constructively interfere with each other, leading to an enhancement in the ionization yield [19,21]. The third plateau, which ranges from 30 to 50 eV, corresponds to elastic backscattering of the electron off the parent ion. This plateau has a cutoff energy of $10.007U_p$ due to the maximum classical energy that a backscattered electron can have [17].

In Fig. 5, the experimental data show a $10U_p$ value of ≈40 eV, which is smaller than that of the deconvolution (≈45 eV). This can be explained by the fact that the peak intensity for each of our Gaussian beams has the smallest three-dimensional volume. In our case, we can verify this explicitly by calculating the volume elements of the beams at each peak intensity [Eq. (5)]. Figure 6 shows density plots of the ATI spectra as a function of the electron energy (horizontal axis) and laser intensity (vertical axis). The dotted curves drawn on top of the density plots are the $2U_p$ and $10U_p$ cutoff energies calculated from the formula,

$$U_p\,(\mathrm{eV}) = 9.33 \times 10^{-14} I_0(\mathrm{W/cm^2})\lambda^2(\mu\mathrm{m^2}), \qquad (9)$$

where λ is the center wavelength in micrometers, I_0 is the intensity in $\mathrm{W/cm^2}$, and the resulting ponderomotive energy has units of eV. For our raw experimental data [Fig. 6(a)], the measured $2U_p$ and $10U_p$ values for each intensity were smaller than the values calculated with the DDAR algorithm. This discrepancy could not be removed by adjusting the intensity calibration by a scaling factor. The deconvolution, however, gives good agreement with the calculated cutoff energies [Fig. 6(b)]. So, even though the ionization probability is, in general, higher for larger intensities, the ionization contributions from intensities slightly lower than the peak value can significantly change the spectrum due to their larger volumes. This is important because it means that the peak intensity and energy of a laser pulse cannot be calculated directly from volume integrated data using the cutoff energies of the spectrum. It should also be noted that none of the spectra from the set of raw data show as much contrast in the ATI peaks as the deconvoluted energy spectra.

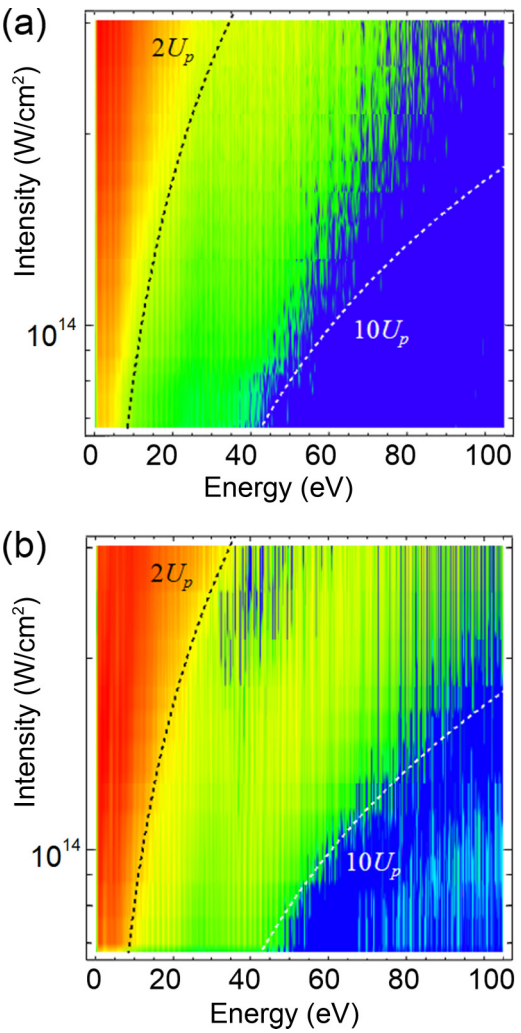

FIG. 6. (Color online) Density plots of the ATI spectra as a function of energy (horizontal axis) and intensity (vertical axis). In both graphs, the $2U_p$ and $10U_p$ cutoff energies for each intensity are denoted by the dotted black and white lines, respectively. (a) The density plot of the experimental data shows a discrepancy between the calculated cutoff energies and the measured ones. (b) The deconvolution of the experimental data recovers the calculated cutoff energies and suggests a better agreement with theory [17].

V. CONCLUSION

The volume integration in the laser focus reduces the intensity resolution of an experimental measurement. Therefore, we developed a DDAR algorithm and applied it to the xenon photoelectron yield to obtain ionization probabilities and intensity-resolved ATI spectra. Our results show that both single- and double-ionization probabilities can be retrieved by inverting the electron yield with DDAR. The retrieved Xe^+ ATI spectrum showed sharper peaks throughout the entire energy range compared to the directly measured one. The $2U_p$ plateau region where femtosecond pulse ionization from Rydberg states is known to dominate the spectrum also shows increased contrast after application of the algorithm.

Applying the DDAR algorithm also recovered $2U_p$ and $10U_p$ cutoff energies that are in excellent agreement with theory, whereas, the experimental data are not. In the latter, intensities that are below the peak intensity can dominate the ATI spectrum due to their much larger differential volumes. Consequently, this leads to a discrepancy between the intensity predicted from the $10U_p$ cutoff energy and the actual peak intensity. This discrepancy cannot be removed by rescaling the intensity calibration by a multiplicative factor. Therefore, we found that the unwanted volume averaging effect can lead to an underestimation of the $10U_p$ cutoff energy (and this discrepancy grows with increasing intensity) by as much as 30%.

ACKNOWLEDGMENTS

This work was funded by the Robert A. Welch Foundation Grant No. A1546 and the Qatar Foundation under Grants No. NPRP 5-994-1–172 and No. NPRP 6-465-1-091.

APPENDIX A: ONE-DIMENSIONAL ILLUSTRATION OF THE DECONVOLUTION ALGORITHM

As an example, let us consider a one-dimensional case when an experiment is performed at two ($N = 2$) different laser peak intensities $I_1 > I_2$ and the volume elements are $V_{1,1}$, $V_{1,2}$, and $V_{2,2}$ (see Fig. 7). Using Eq. (3), the measured ion count rates for beams (a) and (b), respectively, in Fig. 7 are then approximated by

$$Y(I_1) = V_{1,2}P(I_2) + V_{1,1}P(I_1), \tag{A1}$$

$$Y(I_2) = V_{2,2}P(I_2). \tag{A2}$$

Since the quantities $Y(I_1)$ and $Y(I_2)$ are measured and $V_{1,1}$, $V_{1,2}$, and $V_{2,2}$ are known from the focal geometry, it is purely a mathematical exercise to solve Eqs. (A1) and (A2) for $P(I_1)$ and $P(I_2)$,

$$P(I_1) = \frac{1}{V_{1,1}}\left(Y(I_1) - \frac{V_{1,2}}{V_{2,2}}Y(I_2)\right), \tag{A3}$$

$$P(I_2) = \frac{Y(I_2)}{V_{2,2}}. \tag{A4}$$

For the general case of N different laser peak intensities, Eq. (3) produces a system of linear equations,

$$\begin{pmatrix} V_{1,1} & V_{1,2} & \cdots & V_{1,N} \\ 0 & V_{2,2} & \cdots & V_{2,N} \\ \vdots & \cdots & \ddots & \vdots \\ 0 & 0 & \cdots & V_{N,N} \end{pmatrix} \begin{pmatrix} P(I_1) \\ P(I_2) \\ \vdots \\ P(I_N) \end{pmatrix} = \begin{pmatrix} Y(I_1) \\ Y(I_2) \\ \vdots \\ Y(I_N) \end{pmatrix}, \tag{A5}$$

or $\hat{V} \cdot \boldsymbol{P} = \boldsymbol{Y}$, where $\hat{V}$ denotes the differential volume matrix, $\boldsymbol{P}$ is the probability array, and $\boldsymbol{Y}$ is the signal yield array. To find the probability $\boldsymbol{P}$, we multiply both sides of Eq. (A5) by the inverse volume matrix $\hat{V}^{-1}$ to obtain

$$\boldsymbol{P} = \hat{V}^{-1} \cdot \boldsymbol{Y}. \tag{A6}$$

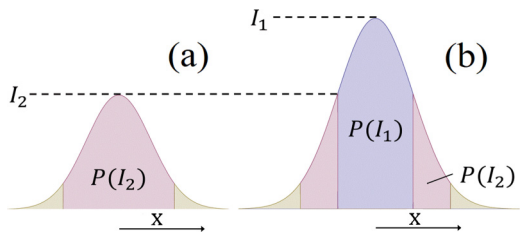

FIG. 7. (Color online) A one-dimensional illustration of Gaussian beams showing the relationship between the volume elements $(V_{1,1}, V_{1,2}, V_{2,2})$ and their respective probabilities $[P(I_1), P(I_2)]$. Regions within the beams with an ionization probability of $P(I_1)$ are colored blue, whereas, regions with probability $P(I_2)$ are colored red. Beam (a) is represented by Eq. (A2). The differential volume of the red region is denoted by $V_{2,2}$. Beam (b) is represented by Eq. (A1). Here the differential volume of the red region is denoted by $V_{1,2}$, and that of the blue region is denoted by $V_{1,1}$. The gold outer wings of each beam are neglected in Eqs. (A1) and (A2).

In general, the volume matrix encodes the experimental setup into the deconvolution algorithm. It is implicitly dependent on the optical elements in the beam path. Therefore, by computing the appropriate volume matrix elements, the algorithm Eq. (A6) can be used to deconvolve data from experiments with a variety of laser beam modes (Gaussian, Laguerre, Gaussian, Hermite-Gaussian, Bessel, etc., . . .).

APPENDIX B: PROCEDURE FOR THE REGULARIZATION ALGORITHM

In practice, the inversion of Eq. (A6) is notoriously unstable, and it is common to remove statistical outliers from the data to improve the algorithm's stability. Here we employ an L^2 norm modification of the variation minimization algorithm proposed by Le *et al.* [13] and expanded by Chartrand and Wohlberg [14]. Generally, L^2 regularization involves the minimization of the dot product $|\boldsymbol{A}|^2$ of a vector $\boldsymbol{A}$, whereas, L^1 regularization refers to the minimization of the absolute value $|\boldsymbol{A}|$. For convenience of notation, we will represent the ionization yields and probabilities in the following way:

$$Y_n \equiv Y(I_n), \quad P_s \equiv P(I_s). \tag{B1}$$

From Bayes' theorem, the probability of having a statistical mean $\bar{Y}_n$ given that we measure a yield Y_n can be expressed as

$$\text{Prob}(\bar{Y}_n|Y_n) = \frac{\text{Prob}(Y_n|\bar{Y}_n)\text{Prob}(\bar{Y}_n)}{\text{Prob}(Y_n)}, \tag{B2}$$

where $\text{Prob}(B)$ is the probability of obtaining B and $\text{Prob}(A|B)$ is the probability of obtaining A given that we know B. Since Y_n, the measurement, cannot be changed, maximizing $\text{Prob}(\bar{Y}_n|Y_n)$ requires ascertaining the appropriate $\bar{Y}_n$. Maximizing $\text{Prob}(\bar{Y}_n|Y_n)$ is, therefore, equivalent to maximizing $\text{Prob}(Y_n|\bar{Y}_n)\text{Prob}(\bar{Y}_n)$. The data Y_n are measured over a fixed interval of time satisfying Poisson statistics. Therefore, the probability of measuring Y_n, provided a mean $\bar{Y}_n$, is given by the Poisson probability mass function,

$$\text{Prob}(Y_n|\bar{Y}_n) = \frac{e^{-\bar{Y}_n}\bar{Y}_n^{Y_n}}{Y_n!}. \tag{B3}$$

The regularization of the data typically is introduced through the probability $\text{Prob}(\bar{Y}_n)$. However, it is more useful to regularize the output of the deconvolution algorithm $\bar{\boldsymbol{P}}$ since this is where the propagated error tends to be the largest. Consequently, the function $\text{Prob}(\bar{Y}_n)$ is replaced by a suitable function $\text{Prob}(\bar{P}_n)$. This function must be chosen based upon experimental constraints. Assuming the derivative of the ionization probability to be continuous, we chose

$$\text{Prob}(\bar{P}_n) = \exp(-\beta(\nabla_{n,s}\bar{P}_s)^2), \tag{B4}$$

where the local derivative,

$$|\nabla_{n,s}\bar{P}_s| \approx \left|\frac{\partial \bar{P}}{\partial I}\right|_n \tag{B5}$$

is with respect to the array variable I, and β is the regularization parameter. The choice of β is discussed in

Sec. IV. Since we ultimately seek the statistical mean of the ionization probability $\bar{\boldsymbol{P}}$, we eliminate the yield mean by the substitution,

$$\bar{\boldsymbol{Y}} \rightarrow \hat{V}\,\bar{\boldsymbol{P}}. \tag{B6}$$

We can now maximize Eq. (B2) by minimizing the negative logarithm,

$$\begin{aligned} &-\ln\left(\mathrm{Prob}(Y_n|\bar{Y}_n)\mathrm{Prob}(\bar{P}_n)\right) \\ &= \bar{Y}_n - Y_n \ln(\bar{Y}_n) + \ln(Y_n!) + \beta(\bar{Y}_n)^2 \\ &= V_{n,s}\bar{P}_s - Y_n \ln(V_{n,s}\bar{P}_s) + \ln(Y_n!) + \beta(\nabla_{n,s}\bar{P}_s)^2. \end{aligned} \tag{B7}$$

Equation (B7) can be viewed as a mechanical action from which we derive the Euler-Lagrange equation with respect to the variables $\bar{P}_s$ and $\nabla_{n,s}\bar{P}_s$, resulting in

$$\hat{V}^T \frac{\hat{V}\,\bar{\boldsymbol{P}} - \boldsymbol{Y}}{|\hat{V}\,\bar{\boldsymbol{P}}|} - 2\beta\hat{\nabla}^2\bar{\boldsymbol{P}} = 0. \tag{B8}$$

It should be noted that, in Eq. (B8), $\hat{M} \equiv \left|\hat{V}\,\bar{\boldsymbol{P}}\right|$ is a diagonal matrix whose elements are as follows:

$$M_{n,m} = \begin{cases} V_{n,s}\bar{P}_s \rightarrow n = m, \\ 0 \rightarrow n \neq m. \end{cases} \tag{B9}$$

This $\hat{M}$ has the general effect of rescaling the regularization parameter $\beta\,(I_n) = \beta M_{n,n}$ to accommodate the variation in the Poisson noise. Because $\hat{M}$ is a function of $\bar{\boldsymbol{P}}$ (and $\bar{\boldsymbol{P}}$ is the desired quantity), $\hat{M}$ will have to be approximated through an iterative process. If the experimental data are taken such that the measurement approximates the statistical mean $\boldsymbol{Y} \approx \bar{\boldsymbol{Y}} = \hat{V}\,\bar{\boldsymbol{P}}$, we can approximate Eq. (B9) by setting the initial value $\hat{M}_0 = |\boldsymbol{Y}|$ and solving for the probability $\bar{\boldsymbol{P}}_i$,

$$\bar{\boldsymbol{P}}_i = (\hat{V}^T\hat{V} - 2\beta\hat{M}_i\hat{\nabla}^2)^{-1}\hat{V}^T\boldsymbol{Y}, \tag{B10}$$

$$\hat{M}_{i+1} = |\hat{V}\,\bar{\boldsymbol{P}}_i|. \tag{B11}$$

Equations (B10) and (B11) are iterated until convergence ($|\bar{\boldsymbol{P}}_i - \bar{\boldsymbol{P}}_{i+1}| < |\bar{\boldsymbol{P}}_{i+1}|/10^4$) is obtained for every element of the vector $\bar{\boldsymbol{P}}_{i+1}$. For our data, only two iterations were needed for convergence. In Eq. (B11), the initial $\hat{M}_i$ $(i = 0)$ is the diagonal matrix of the measured yields,

$$|\boldsymbol{Y}| = \begin{pmatrix} |Y_1| & 0 & \cdots & 0 \\ 0 & |Y_2| & 0 & \vdots \\ \vdots & 0 & \ddots & 0 \\ 0 & 0 & 0 & |Y_n| \end{pmatrix}, \tag{B12}$$

and $\hat{\nabla}^2$ is the second derivative matrix. We found the second derivative by multiplying two first derivative matrices defined by

$$\hat{\nabla} = \frac{1}{\Delta I}\begin{pmatrix} 1 & -1 & 0 & \cdots & 0 \\ 0 & 1 & -1 & 0 & \cdots \\ \cdots & 0 & 1 & \ddots & 0 \\ \cdots & \cdots & 0 & \ddots & -1 \\ 0 & \cdots & \cdots & 0 & 1 \end{pmatrix}. \tag{B13}$$

In general, the intensity spacing $\Delta I = I_i - I_{i+1}$ is not constant and should be calculated for each row of the derivative matrix. We refer to the initialization step along with the iteration of Eqs. (B10) and (B11) and the convergence criterion as the DDAR algorithm.

[1] S. Larochelle, A. Talebpour, and S. L. Chin, J. Phys. B **31**, 1201 (1998).

[2] P. Lambropoulos, X. Tang, H. Xu, W. Nicklich, H. Kumpfmüller, and H. Walther, in *Structure in the Above Threshold Ionization (ATI) Spectrum and Off-Resonance Rabi-Like Oscillations under Strong Femtosecond Pulses*, edited by H. Walther, T. W. Hänsch, and B. Neizert, AIP Conf. Proc. No. 275 (AIP, New York, 1993), p. 499.

[3] J. Strohaber and C. J. G. J. Uiterwaal, Phys. Rev. Lett. **100**, 023002 (2008).

[4] K. J. Schafer and K. C. Kulander, Phys. Rev. A **42**, 5794 (1990).

[5] E. Cormier and P. Lambropoulos, J. Phys. B **30**, 77 (1997).

[6] P. Hansch and L. D. Van Woerkom, Opt. Lett. **21**, 1286 (1996).

[7] M. A. Walker, P. Hansch, and L. D. Van Woerkom, Phys. Rev. A **57**, R701 (1998).

[8] W. A. Bryan, S. L. Stebbings, E. M. English, T. R. Goodworth, W. R. Newell, and J. McKenna *et al.*, Phys. Rev. A **73**, 013407 (2006).

[9] T. R. J. Goodworth, W. A. Bryan, I. D. Williams, and W. R. Newell, J. Phys. B **38**, 3083 (2005).

[10] M. Schultze, B. Bergues, H. Schröder, F. Krausz, and K. L. Kompa, New J. Phys. **13**, 033001 (2011).

[11] J. Strohaber, A. A. Kolomenskii, and H. A. Schuessler, Phys. Rev. A **82**, 013403 (2010).

[12] R. W. Boyd, *Nonlinear Optics* (Academic, Waltham, MA, 2008).

[13] T. Le, R. Chartrand, and T. Asaki, J. Math. Imag. Vision **27**, 257 (2007).

[14] R. Chartrand and B. Wohlberg, *2010 IEEE International Conference on Acoustics Speech and Signal Processing (ICASSP), Dallas, 2010* (IEEE, Piscataway, NJ, 2010), pp. 766–769.

[15] S. Speiser and J. Jortner, Chem. Phys. Lett. **44**, 399 (1976).

[16] A. M. Perelomov, V. S. Popov, and M. V. Terent'ev, J. Exptl. Theoret. Phys. **50**, 1393 (1966) [Sov. Phys. JETP **23**, 924 (1966)].

[17] G. G. Paulus, W. Becker, W. Nicklich, and H. Walther, J. Phys. B **27**, L703 (1994).

[18] T. J. McIlrath, R. R. Freeman, W. E. Cooke, and L. D. van Woerkom, Phys. Rev. A **40**, 2770 (1989).

[19] G. G. Paulus, F. Grasbon, H. Walther, R. Kopold, and W. Becker, Phys. Rev. A **64**, 021401 (2001).

[20] R. Kopold, W. Becker, M. Kleber, and G. G. Paulus, J. Phys. B **35** 217 (2002).

[21] G. G. Paulus, F. Grasbon, A. Dreischuh, H. Walther, R. Kopold, and W. Becker, Phys. Rev. Lett. **84**, 3791 (2000).